International Journal of Mechanical Sciences 296 (2025) 110344

Contents lists available at ScienceDirect

International Journal of Mechanical Sciences

journal homepage: www.elsevier.com/locate/ijmecsci

Tensegrity-inspired sandwich metamaterial for reprogrammable stiffness and impact mitigation

Bowen Tan, Bushra Jawed, Ke Liu *

School of Advanced Manufacturing and Robotics, Peking University, Beijing 100871, China

A R T I C L E I N F O

Keywords:
Mechanical metamaterials
Tensegrity structures
Reprogrammable stiffness
Load bearing
Impact mitigation

A B S T R A C T

Metamaterials are renowned for their unique properties, but most have fixed properties once fabricated. Tensegrity metamaterials offer tunable mechanical properties by adjusting prestress, making them excellent for load-bearing and energy absorption. However, tensegrity structures' inherent self-equilibrium and stability demand complex geometries with irregular angles and pre-tensions, restricting convenient fabrication. To address those limitations, we propose a tensegrity-inspired sandwich metamaterial (TSM), which preserves the stress redistribution capability of standard tensegrity structures, yet can be easily fabricated. The design comprises an elastic membrane sandwiched by two spiked plates, with the membrane in tension and the spikes in compression. The TSM can be reprogrammed to achieve a wide range of static and dynamic responses by adjusting the preloading distance between the two plates. In particular, the TSM achieves a tuning of energy dissipation efficiency within the range of 20%-56% and the tuning of mitigation rate in the range of 0.136-0.204 by a single layer. This study provides a pathway for creating effective and reprogrammable energy-absorbing metamaterials for impact mitigation systems, allowing for active control of static and dynamic responses.

1. Introduction

Tensegrity is typically recognized as pin-connected frameworks with cables and struts [1–3]. Cables form a continuous tensile network, and struts are discretely encompassed into the tensile network to resist compressive forces [4]. The documentation of tensegrity can be traced back to a century ago [5]. Initially, it was a type of architecture that attained rigidity with a combination of compression and tension elements [6,7]. Unlike truss structures, each element in a tensegrity structure only bears tension or compression load without suffering from bending and shear loads [8]. Thus, the tensegrity structure possesses significant potential to avoid early localized failure [9], making it well-suited for impact absorption applications [10]. Moreover, tensegrity structures exhibit excellent properties, such as high stiffness-to-mass ratio, lightweight, programmable deployment, reprogrammability, and substantial load-bearing capacity [11–14]. These have been applied in various fields, including sculpture, biomedical devices, robotics, and space structures [15–19].

Compared with lattice metamaterials [20–22], the construction of tensegrity structure is more complex [23–25]. It relies on the balance of forces to maintain its shape and function rather than on rigid connections. Stability under prestress is the most critical characteristic of a tensegrity structure that must be satisfied [26–28]. The generalized concept of tensegrity is defined as any prestressed structural system that is stable with continuous tensile components [29]. As long as the balance between prestress tension and compression is maintained, most of the excellent properties of tensegrity are preserved [30–35]. However, the design and fabrication of tensegrity structures have long been a major challenge, owing to the stringent geometric, assembly, and prestress requirements [36–39]. This procedure requires a high level of accuracy since a given structure's statics greatly depend on the specific level of prestress in the tensioned and compressed members [40–42]. Manufacturing and assembly errors significantly affect the stability of the tensegrity structure and may even cause failure [43–46]. The initial imperfections may also reduce the performance of the tensegrity [44].

The unique self-stress state endows the tensegrity structures with the ability to control their mechanical properties [47]. This had an important application for controlling wave propagation, like absorbing the energy of compression waves [48,49], tuning the propagation velocity [50–52] and bandgap range [53–55]. Yin [56] designed a truncated regular octahedral tensegrity-based metamaterial and tuned the Poisson's ratio in a wide positive/negative range by prestressing. Whereas,

* Corresponding author.
E-mail address: liuke@pku.edu.cn (K. Liu).

https://doi.org/10.1016/j.ijmecsci.2025.110344
Received 13 January 2025; Received in revised form 29 April 2025; Accepted 2 May 2025

Salahshoor [57] studied the material symmetry phase transitions of tensegrity lattice and achieved several phase transitions due to cable prestressing. On the other hand, Li [58] proposed a configurable tensegrity-based metastructure with rigidity-flexibility phase transition and exhibits rich bandgap turning. Although the conceptual designs of tensegrity metamaterial demonstrate great theoretical potential, they have not been actualized except for one-dimensional chains [59–61]. Nevertheless, the implementation and tuning of prestress are still challenging because the members are unstable until the assembly is finished, and prestress forces may deviate [62,63]. The critical buckling load in struts also limits the level of prestress. Liu [64] further discussed tuning stiffness of tensegrity-based metamaterial by prestressing. Tuning stiffness may potentially affect impact mitigation, yet this has not been explored.

In impact mitigation, when observed in lattice materials, localized deformation could significantly decrease the energy absorption [65] and the vibration fatigue life [66,67]. In contrast, the continuous network of tensegrity structures provides a redundant path for transferring loads and deformation [68], so it has the advantage of passively dissipating energy [69]. Bauer [70] proposed a space tessellating tensegrity metamaterial with delocalized deformation and experimentally confirmed that energy absorption can meet the level of other types of metamaterials. Yang [71] proposed a bistable tensegrity structure with superior reusability, achieving high energy absorption. Zhang [72] made a tensegrity protective drone shell that showed good mitigation for collision dynamics. Some efforts for improving the energy-absorbing capabilities have also been proposed, like adding the bar bucking energy [10,73], increasing the number of unit cells [74], enhancing prestress level [75], and filling with metal rubber [76].

This study aims to examine the tunability of tensegrity structure on static stiffness and impact mitigation. A novel type of tensegrity structure is proposed to increase the tunable range, which looks like a sandwich structure, hence named tensegrity-inspired sandwich metamaterial (TSM). The structural complexity has been dramatically simplified for easy fabrication and prestress adjustment. TSM can realize a tuning distance of up to 50% of its height. Therefore, using TSM, the relationship between tuning distance and structural stiffness and the effect on impact mitigation was investigated. The structure of the paper is organized as follows. Section 2 introduces the geometric design of the TSM, numerical simulation setups, and an analytical model for static behavior. Section 3 presents the quasi-static simulation results of the TSM, showcasing the reprogrammable mechanical properties, load distribution capability, and impact mitigation performance. Section 4 summarizes the main observations of the study.

2. Material and method

This section provides details on the design of the TSM unit cells and the assembly strategy. Next, material and numerical simulation models are introduced. Additionally, an analytical model is proposed to predict the compression behavior of the TSM.

2.1. Design of TSM

The TSM unit cell comprises struts, membranes, and cables, as shown in Fig. 1 (a). The struts are fixed vertically on the top and bottom plates, forming two spiked plates. The top and bottom struts are staggered, so the load must transfer through the membrane, avoiding direct contact between the struts. Thus, the elastic membrane serves as the continuous tensile component and preserves tensegrity features. The peripheral cables are also part of the continuous tensile components; their length could preload TSM.

Based on the unit cells, a metamaterial can be constructed by tessellation. For instance, Fig. 1 (b) shows a 3 × 3 tessellation of 2D metamaterial. Here, the unit cells are aligned side by side, and merging is done by integrating the bottom plate. After merging, the top struts become 3 × 3, whereas the bottom struts become 4 × 4, placed alternately, as shown in Fig. 1 (c). The membranes are fused into a large membrane to connect all the struts. Compared to traditional tensegrity structures, TSMs are easily assembled by layering three pieces of major components: top plate, membrane, and bottom plate. The membrane could adjust its deformation to accommodate tension in all directions. The eight peripheral cables are incorporated to connect the top and bottom plates that make TSM as a whole. When preloading TSM by decreasing the length of the cables, the struts compress the membrane into a zigzag shape, as shown in Fig. 1 (d). The preloading process forms a prestressed state inside the TSM. The corresponding geometric parameters of a typical TSM are listed in Table 1, which is used for numerical simulations later.

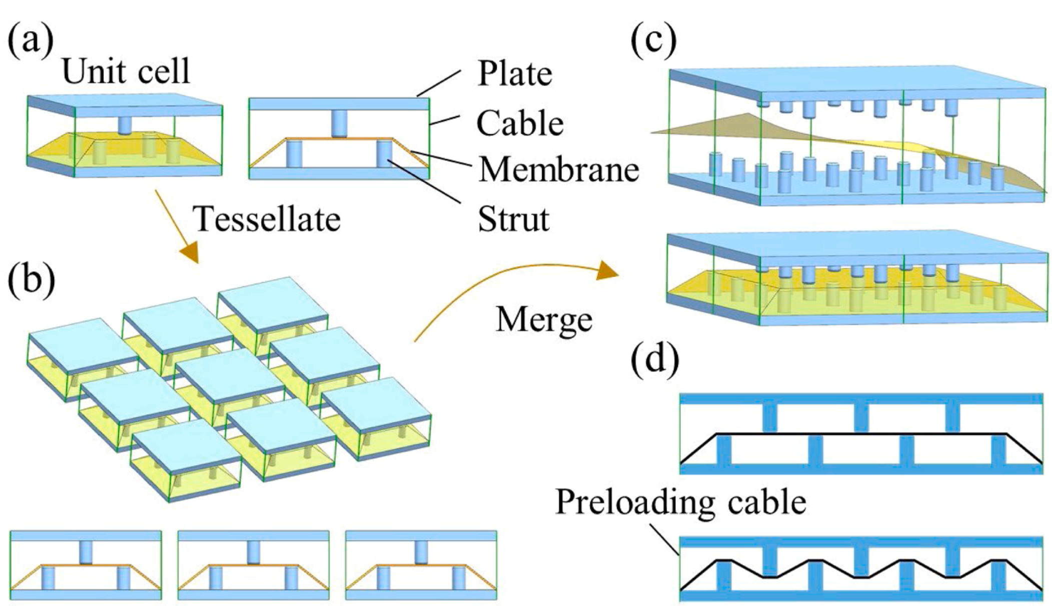

Fig. 1. The structural design of TSM. (a) A unit cell constructed by the tensegrity concept. The unit cell comprises two spiked plates, four cables, and an elastic membrane. (b) A 3 × 3 array tessellation strategy of the TSM. (c) The assembly of metamaterial from unit cells by merging the boundaries. The overlapped cables and portion of the plates and membrane are deleted. (d) Preloading of the TSM through tightening of peripheral cables.

Table 1
The geometric parameters of a TSM design.

Item	Radius (mm)	Height (mm)	Spacing (mm)	Item	Side length (mm)	Thickness (mm)
Top struts	4	7	22.5	Plates	90	3
Bottom Struts	4	7	22.5	Membrane	100	0.5
Cables	0.25	20.5	45			

2.2. Material selection

For the numerical simulations and the example physical model in Fig. 2, PLA was chosen as the material for the two plates. PLA is one of the most common materials for 3D printing because of its processability, low density, and relatively good mechanical properties for load-bearing applications. For the membrane, PDMS was chosen with a thickness of 0.5 mm because it has good strength and toughness. The peripheral cables are chosen as Kevlar ropes because of their high stiffness and tensile strength. The elastic properties of the selected materials are outlined in Table 2.

2.3. Numerical simulation

Finite element simulations by commercial software ANSYS/LSDYNA were carried out to analyze the out-of-plane compressive behavior of TSM. The top and bottom plates with struts are modeled by the 8-node 3D solid elements. The membrane is discretized by the 4-node Belytschko-Tsay membrane shell elements (Type 9) with full integration. The peripheral cables are modeled as discrete beam elements. After the mesh convergence study, we selected a mesh size of 1 for the shell and the solid elements. The membrane, struts, and peripheral cables were connected by node coupling to ensure interfacial compatibility. The material properties summarized in Table 2 were modeled by adopting an isotropic material model (Material Type 1). The preloading of TSM was applied by shrinking the length of the beam elements of peripheral cables.

Table 2
Elastic properties of the material in TSM.

Material	Elastic modulus (Mpa)	Poisson's ratio	Density (g/cm^3)
PLA	2200	0.4	1.05
PDMS	2.3	0.483	1
Kevlar	12670		1.07

Two rigid loading plates (the grey parts in Fig. 3) were used to compress TSM to simulate the quasi-static process. The lower rigid plate was fixed in all directions. The upper rigid plate was fixed in five directions except for the vertical direction, and a constant compressing speed of 25 mm/s was applied. A general contact algorithm was defined between the rigid plates and the plates of TSM. The friction coefficient was set to 0.25. The kinetic to internal energy ratio was limited to be lower than 5% to ensure the compression is a quasi-static process.

The load-displacement curves of TSM by experiment and numerical simulation are compared in Fig. 4, and the results show a good overall agreement. The first 1.5 mm exhibits a zero-stiffness zone. During this period, the membrane is slightly stretched, and the conversion of the tension force into the vertical force is negligible due to the struts being perpendicular to the membrane, as depicted in Fig. 5 (a). As the compression reaches 3 mm (Fig. 5 (b)), the upper and bottom stretch the membrane more and disperse the membrane into equally distributed

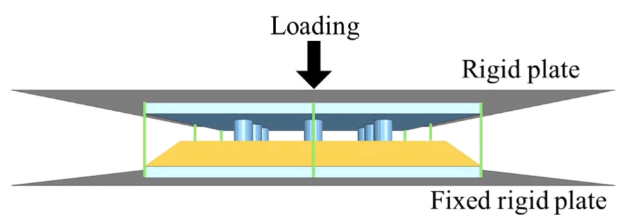

Fig. 3. Finite element model of the TSM. The metamaterial is placed between two rigid plates. The lower rigid plate is fixed. The upper rigid plate is fixed except for the vertical direction. A vertical displacement load is applied on the upper rigid plate.

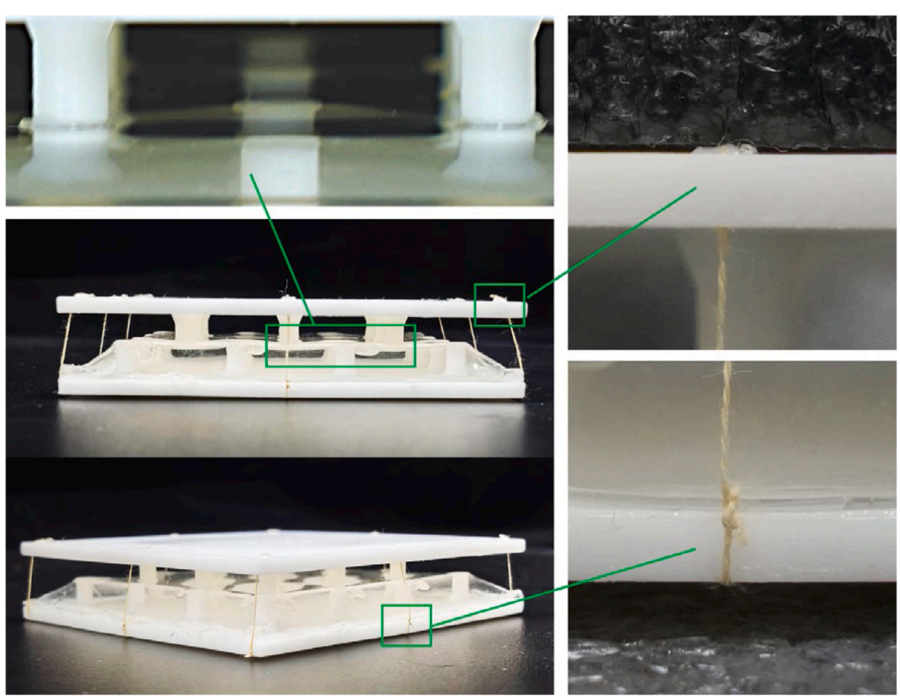

Fig. 2. A physical model of TSM made by spiked plates, membrane, and peripheral cables.

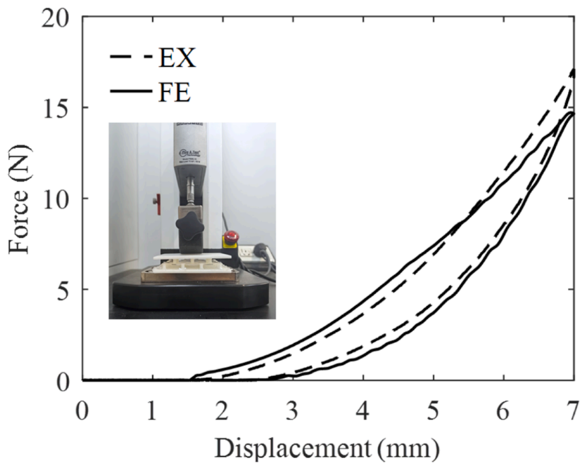

Fig. 4. Comparison of the compressive force-displacement curves of experiment and finite element simulation.

strips and facets. The strips are the direct tension parts and form a continuous network, the width of which is larger than the diameter of the struts. The facets are the indirect tension parts from the interaction between unit cells, with less stretch than strips. As the compression reaches up to 7 mm, the deformation mode of the membrane remains. We can observe that the deformation of unit cells is divided into two types: the peripheral unit cells have less unit cell interaction, and the facet is slightly stretched (type I); the inner unit cells have full interaction, and the facet is stretched large (type II). The strips are not affected by the position.

2.4. Analytical model

The membranes are the dominant deformation component of the TSM and significantly influence the mechanical characteristics of the structure. An analytical model was created to assess the deformation by considering the membrane's elastic deformation while ignoring the small deformations of the relatively rigid spiked plates. Because the membrane is very thin and soft, its bending deformation was not taken into consideration. Therefore, the model only considered in-plane stretching deformation, which is regarded as a tensile network following the tensegrity concept. The assumption helps reduce the complexity of the analytical derivation while providing enough accuracy for evaluating the structure's performance.

As shown in Fig. 6 (a), for a single unit cell, the tension in the membrane is concentrated between the struts as four tensile strips, EA, EB, EC, and ED, indicated by red lines. These tensile strips arise inherently from the geometric layout and can be simplified to linear tensile elements in the analytical model. Each strip is then modeled by a bar element possessing axial stiffness, which offers a relatively accurate approximation of the membrane's tension behavior [77]. When two unit cells are combined, as shown in Fig. 6 (b), an interaction happens between the cells. The area AEBG further generates four secondary tensile strips FA, FB, FE, and FG (blue lines). As line EG moves down following compression of the top struts, line AB tends to remain stationary with the bottom struts, so they stretch each other and generate a balance point F. On this foundation, an analytical model was built for TSM, as shown in Fig. 6 (c). The analytical model comprises two tensile networks inside and between the unit cells.

The derivation of the analytical model is based on the linear-elastic material model ($\sigma = E\varepsilon$). It is assumed that the ends of the bar elements are fixed to struts. Specifically, the ends on the bottom structure remain stationary, while those on the upper struts move in response to compression. The analytical model is calculated using an explicit method.

The axial stiffness of the bar element is defined as [36]:

$$k_{bar} = \frac{E_m A_e}{L}, \tag{1}$$

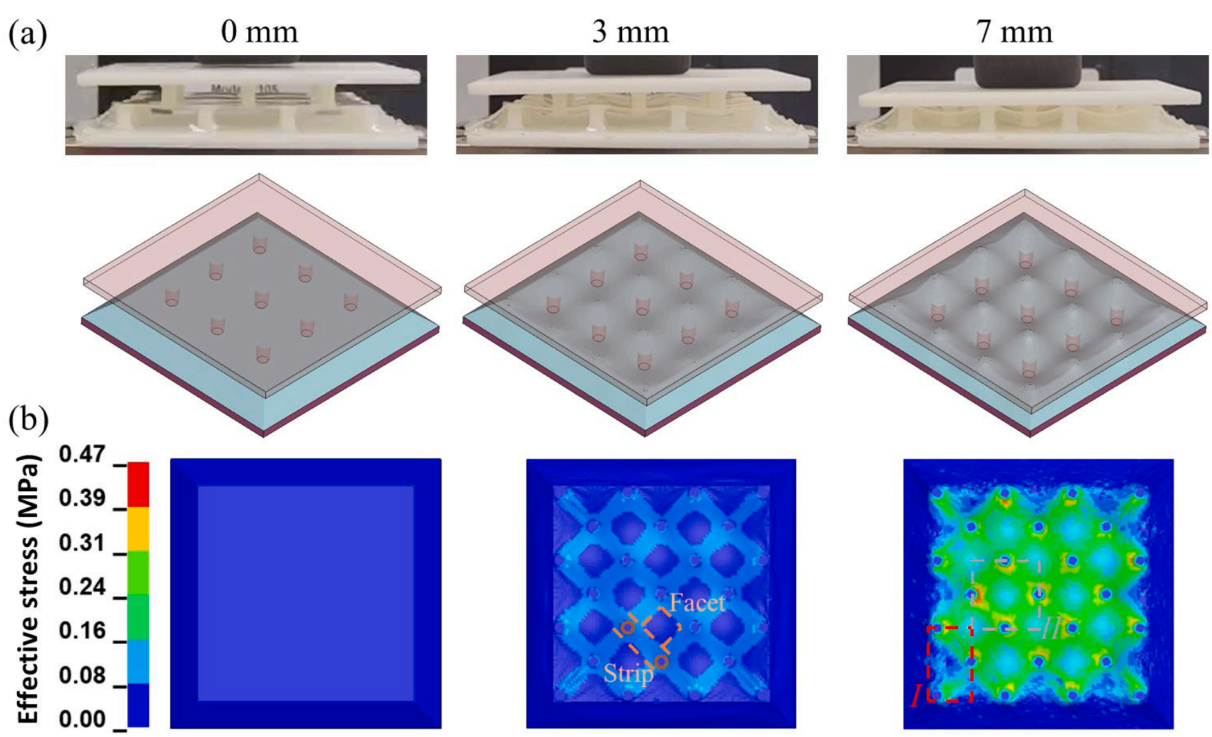

Fig. 5. Deformation mode of TSM. (a) Deformation mode at different amounts of compression. (b) The von Mises stress distribution in the membrane - a tension network is formed. Orange boxes highlight the strips and facets of the membrane's deformation patterns. Red and grey boxes show peripheral and internal unit cells (type I and II).

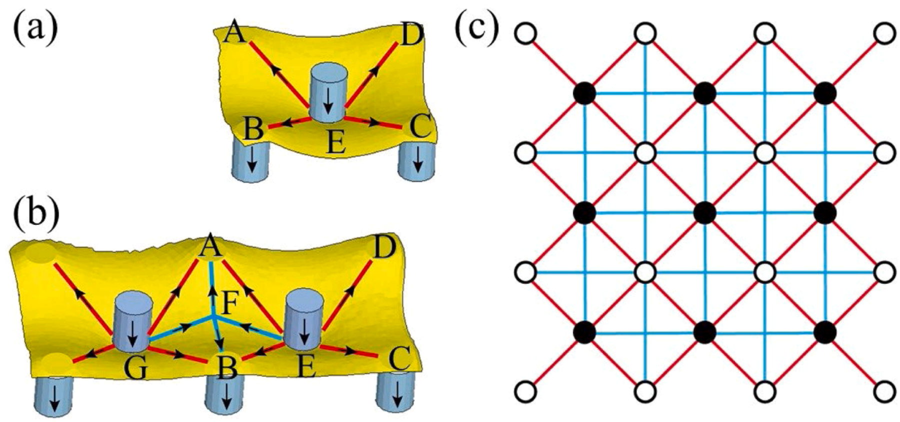

Fig. 6. Schematic of the analytical model for (a) a unit cell and (b) two adjacent unit cells. The arrows denote the direction of force transmission. For one unit cell, the deformation of the membrane is simplified as four tension bars (red line). For two unit cells, four additional tension bars (blue line) are generated between unit cells. (c) The simplified tension network structure of the entire membrane. Filled and hollow circles were used to represent the top and the bottom struts, respectively.

where E_m is the elastic modulus of the membrane, A_e is the effective area and L is the initial length of the equivalent virtual bar.

The basic deformation energy function of one bar element in the tensile network is assumed to be:

$$U = \frac{1}{2}k_{bar}\Delta l^2 = \frac{1}{2}\frac{E_m A_e}{L}\Delta l^2 = \frac{E_m A_e}{2}\left(L\varepsilon^2\right), \tag{2}$$

where ε is the linear strain and $\varepsilon = \Delta l/L$.

The definition of bar area needs to consider the strut diameter and the surface deformation of the membrane. The width of the tension strips is larger than the struts' diameter. The effect is estimated by introducing Poisson's effects for tensile loading. The bar areas are then defined as:

$$A_e = t(1 + 2\upsilon)D, \tag{3}$$

where t is the membrane thickness, and D is the strut diameter.

The length of the bar elements during compression is a function of displacement. For the network connecting struts directly (red network), the length is $l_{EA} = \sqrt{\delta^2 + L_{EA}^2}$. For the network between unit cells (blue network), the length is $l_{FA} = \sqrt{(\delta/2)^2 + L_{FA}^2}$. As parts of the membrane are fixed onto the end of the struts and not deformed, the bar length needs to remove this part. The bar length is then defined as:

$$L' = L - D \text{ and } l' = l - D. \tag{4}$$

The strain of the bar element is defined as [54]:

$$\varepsilon = \frac{l' - L'}{l'}. \tag{5}$$

Thus, the deformation energy stored in TSM is given by:

$$U = \frac{EA_e}{2}\left(N_1 L'_{EA}\varepsilon_{EA}^2 + N_2 L'_{FA}\varepsilon_{FA}^2\right) = \frac{EA_e}{2}\left(N_1(L_{EA} - D)\left(\frac{\sqrt{\delta^2 + L_{EA}^2} - L_{EA}}{\sqrt{\delta^2 + L_{EA}^2} - D}\right)^2 + N_2(L_{FA} - D)\left(\frac{\sqrt{(\delta/2)^2 + L_{FA}^2} - L_{FA}}{\sqrt{(\delta/2)^2 + L_{FA}^2} - D}\right)^2\right), \tag{6}$$

where, N_1 and N_2 are the number of bars in the two layers of the network, respectively. N_1 and N_2 are related to the number of unit cells $\widehat{N}$. $N_1 = 4\widehat{N}$ and $N_2 = 4(2\widehat{N} - m_c - 0.5m_s)$, here m_c and m_s are the number of unit cells at the corner and side, respectively. For the current TSM, m_c=4 and m_s=4, so that N_1=36 and N_2=48.

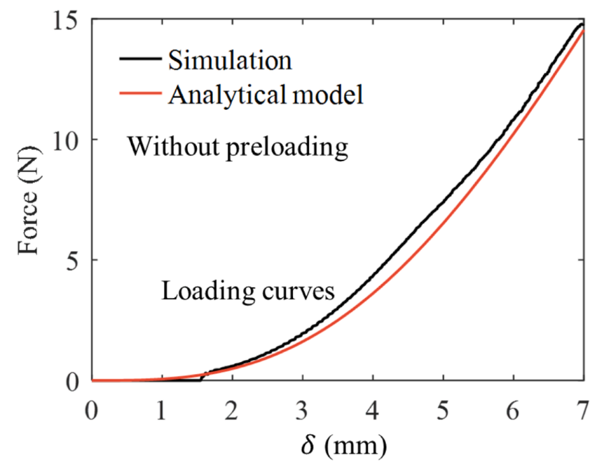

Fig. 7. Comparison of the compressive force-displacement curves of the finite element simulation and the analytical model.

The compression force of TSM corresponding to displacement δ is derived by

$$F = \frac{dU}{d\delta}. \tag{7}$$

A comparison of the results from a numerical simulation and the analytical model is shown in Fig. 7, without considering prestress. The simplified analytical model provides reasonable estimations for the mechanical behavior of the TSM under compression.

When TSM is preloaded by $\widehat{\delta}$ to induce prestress, if the peripheral cables are rigid, the force-displacement curve of TSM could be translated from the original curve (Fig. 8):

$$F = F(\delta + \widehat{\delta}). \tag{8}$$

However, the peripheral cables are not rigid. When considering the

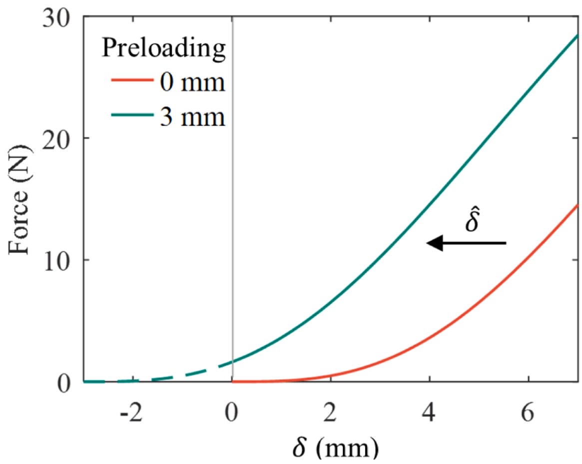

Fig. 8. Effect of preloading distance $\hat{\delta}$ on the compressive force-displacement curves of TSM, calculated from the analytical model, without preloading.

peripheral cables' deformation, they elongate Δl_c after preloading. Therefore, the initial compression of TSM first leads to slackness of the elongated cables. The axial stiffness of the peripheral cables is defined as [36]:

$$k_c = \frac{E_c A_c}{L_c - \hat{\delta}}, \tag{9}$$

where E_c is the elastic modulus of the cables, A_c is the cross-sectional area, L_c is the initial length of cables without preloading.

The elongation of cables Δl_c is from the equilibrium of forces between the cables and the metamaterial:

$$F(\hat{\delta} - \Delta l_c) = nk_c \Delta l_c, \tag{10}$$

where n is the number of peripheral cables.

The compression force of TSM with preloading is divided into two stages:

$$F = \begin{cases} nk_c\delta, \ \ \delta < \Delta l_c \ \text{(Stage I)} \\ F(\delta + \hat{\delta} - \Delta l_c), \ \ \delta \geq \Delta l_c \ \text{(Stage II)} \end{cases}. \tag{11}$$

A comparison of the results of a numerical simulation and the analytical model is shown in Fig. 9, considering a preloading distance of 3 mm. The analytical model agrees well with the numerical simulation result.

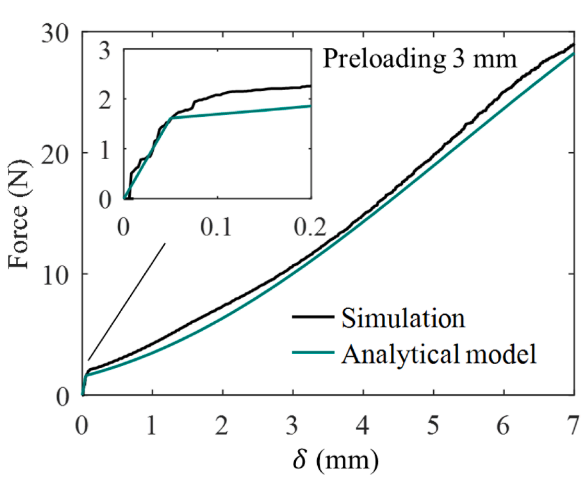

Fig. 9. Comparison of the compressive force-displacement curves of the finite element simulations and the analytical model. A preloading $\hat{\delta}$ of 3 mm is applied.

The elastic modulus k^* of TSM corresponding to displacement δ is derived by

$$k^* = \frac{dF}{d\delta}. \tag{12}$$

Fig. 10 shows the elastic modulus of TSM in response to various material properties and preloading distances. The initial elastic modulus (Stage I) of TSM ($\delta < \Delta l_c$) is only related to the elastic modulus of the peripheral cables E_c. In Stage II, the elastic modulus of TSM dramatically decreases by two orders of magnitude, and Fig. 10 (b) shows the elastic modulus of TSM at $\delta = \Delta l_c$. The preloading distance and the elastic modulus of the membrane E_m effectively tune the elastic modulus of TSM.

3. Results

In this section, the mechanical behavior of TSM is discussed in detail for different loading conditions and preloading distances. The simulations also show the shear deformation behavior of TSM. Furthermore, load distribution capability is examined by localized loading. The final part of this section quantifies the impact mitigation property of the TSM, which is also tunable by modifying the prestress level through preloading.

3.1. Tunable compressive mechanical properties

The simulation of TSM goes through three processes, namely preloading, holding, and loading, as illustrated in Fig. 11 (a). The preloading process is the tuning of TSM. Through shrinking the length of peripheral cables, the prestress is generated and distributed through the entire structure. The prestress increases as the preloading proceeds. In the holding process, the length of peripheral cables is no longer changed, and the prestress is maintained in the structure, as shown in Fig. 11 (b). Then, the loading process is the formal application of TSM. As mentioned above, the internal forces of cables first release sharply and divide the loading process into two stages.

The preloading process of TSM could be seen as a quasi-static compression process. The preloading distance is equivalent to the compression distance. Multiple displacement-controlled loading-unloading cycles with progressively increasing displacement (2, 3, 4, 5, 6, and 7 mm) were performed to measure the mechanical properties, as shown in Fig. 12. When the compression is less than 4 mm, TSM shows an ideal elasticity that the loading and unloading process follows the same curve. Then, TSM exhibits a hysteresis effect when the compression is larger than 4 mm. At this moment, the strains in the membrane are inhomogeneous. When the TSM unloads, the parts with different strains will hinder each other's potential energy release. As the strain of the membrane increases, the hysteresis effect is enhanced.

In the loading process, the force-displacement curves of TSM with different preloading distances are shown in Fig. 13 (a). Stage I is the release of taut cables, so the preloading does not affect the stiffness. The maximum force of Stage I is limited by the cables' prestress. In Stage II, the slope of the curve is determined by the preloading distance. It comes from the change of stretch angle between the struts and membrane. A large stretch angle will increase the strain increment of the membrane and the vertical component forces. The average stiffness of the TSM in Stage II increases as the preloading distance increases. As the preloading distance increases, the linearity of the metamaterial also improves. With a preloading of 5 mm, TSM nearly shows a bilinear force-displacement curve. The hysteresis effect from the preloading process is transferred to the loading process and continues increasing with compression distance. The energy dissipation capability is increased as preloading, as shown in Fig. 13 (b).

In Fig. 14, the effect of the stretch angle of the membrane on the force-displacement curves of TSM was evaluated. The stretch angle of the membrane increases with the preloading distance, which converts

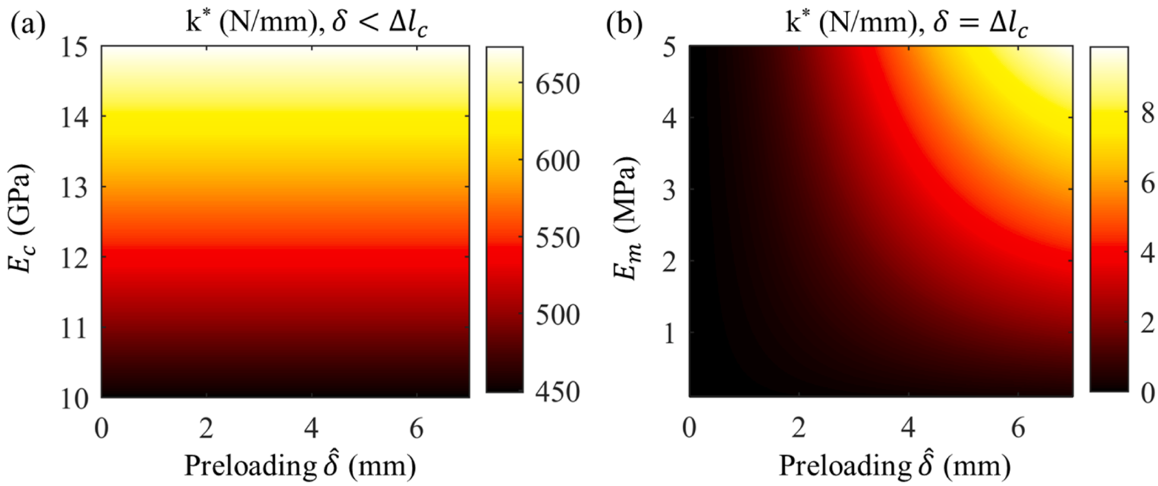

Fig. 10. TSM with tunable elastic properties at the two stages of (a) $\delta < \Delta l_c$ and (b) $\delta = \Delta l_c$.

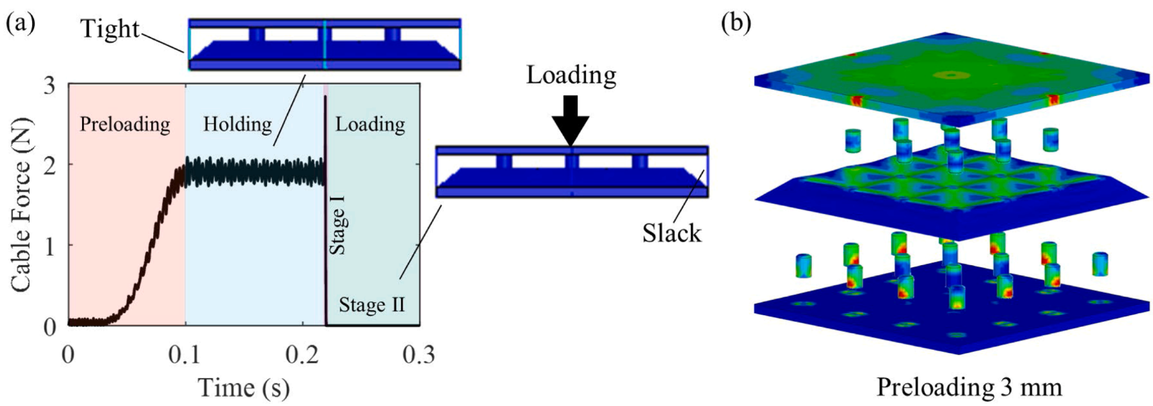

Fig. 11. (a) The internal force of peripheral cables in the three processes of preloading, holding, and loading. (b) Deformed shapes and von Mises stresses of TSM at the holding state with a preloading distance of 3 mm.

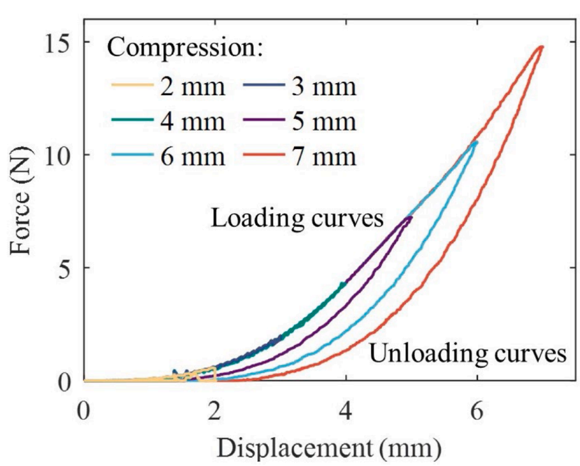

Fig. 12. Force-displacement curves under loading-unloading cycles. The cycle displacement is increased progressively.

more of the membrane's tension to vertical force. However, the maximum stretch angle is limited due to the geometric structure, so the change of stretch angle gradually decreases (Fig. 14 (a)). This is reflected in the linearity of the loading curves increases, as shown in Fig. 14 (b). Thus, the nonlinearity of TSM is a geometric nonlinearity.

3.2. Shear deformation behavior

Shear deformation simulations were carried out to explore the effect of loading direction on the mechanical properties of TSM. The bottom plate was fixed, and the upper plate applied a force in the in-plane direction, as shown in Fig. 15 (a). The force direction was selected as 0°, 15°, 30°, 45°, 60°, 75°, and 90°. Fig. 15 (b) shows the von Mises stress distribution in the membrane. Due to the constraint of peripheral cables, the shear deformation of TSM follows the parallelogram law. The upper plate is always parallel to the bottom plate, so the struts stretch the membrane uniformly. Compared with the out-of-plane deformation, only half of the membrane is tensioning, and the other part compresses to wrinkle. As the force direction changes, the number of tension strips changes from sixteen to nine at 0° and 45°.

In Fig. 15 (c), the shear forces of TSM are compared with the out-of-plane forces. For shear deformation, the force direction and the stretching direction are in the same plane, so the stretching of the strips is more direct. For out-of-plane compression, the declination angle between the compression and stretch directions decreases the compression force. Therefore, when subjected to oblique loading, TSM tends to compress rather than shear, and TSM has a good transverse strength. The shear forces at 0° and 45° are nearly identical. This may be because the surface deformation of the membrane compensates for the influence of the angular change, which is superior to a single tensile network. Therefore, in Fig. 15 (d), the shear moduli of TSM are insensitive to the shear direction, and TSM is transversely isotropic.

The shear moduli can be derived from [78]

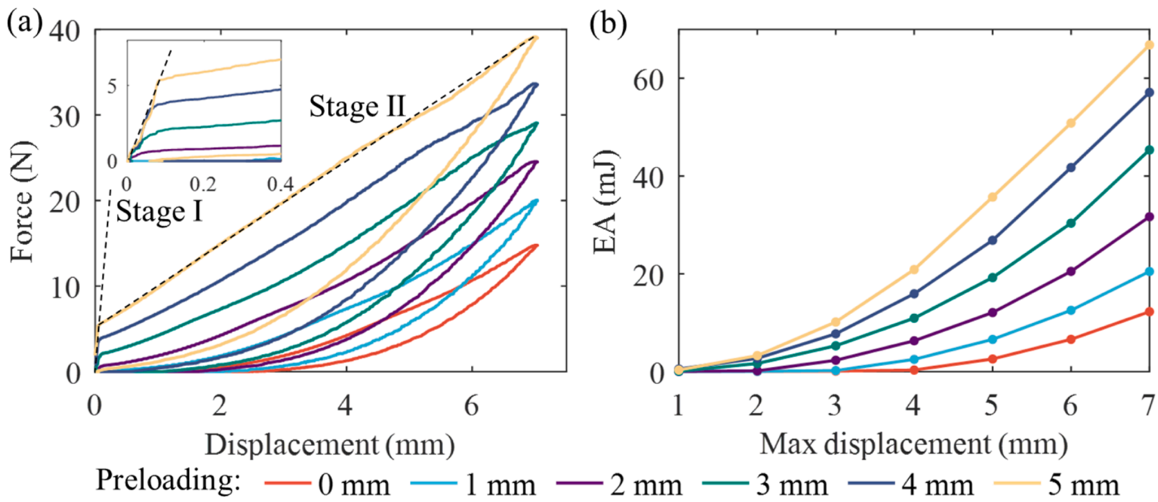

Fig. 13. Reprogrammable static mechanical properties. (a) Force-displacement curves of TSM under different preloading distances. The loading curves are divided into two stages due to preloading. (b) Tunable energy absorption characteristics of TSM.

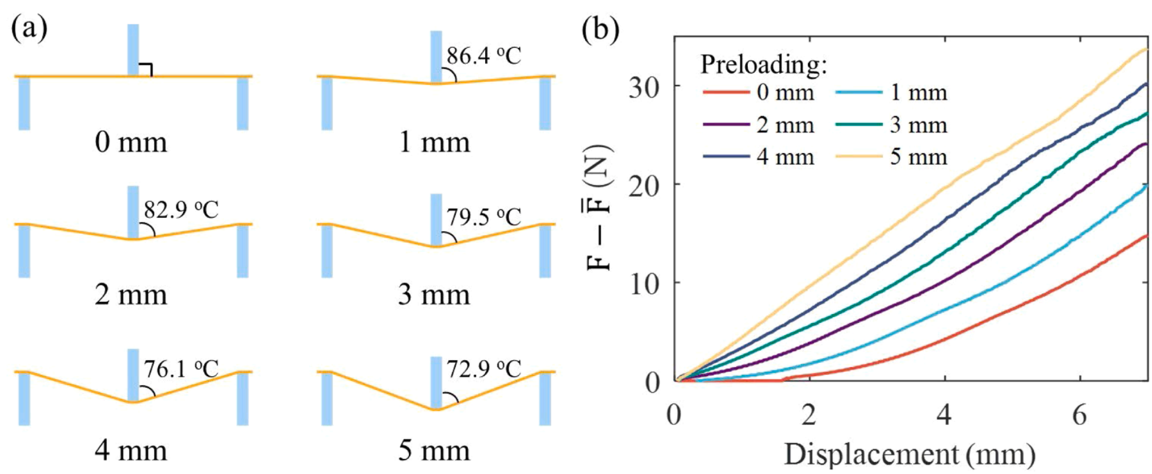

Fig. 14. Geometric nonlinearity of the TSM under compression. (a) Simplified geometrical configurations of the TSM under different preloading. The blue rectangle indicates the struts, and the yellow lines represent the membrane along the diagonals. (b) Force-displacement curves for TSM with different preloading. The curves are subtracted by the cables' force $\overline{F}$ to highlight the impact of large deformation of the membrane.

$$G' = \frac{F_x/A_\mu}{\delta_x/L_\mu}, \tag{13}$$

where F_x and δ_x represent the shear force and displacement, A_μ and L_μ represent the area and width of the plate, respectively.

3.3. Load distribution performance

In Fig. 16, the load distribution capability of TSM was validated compared to a non-tensegrity structure. Here, we applied a point load of 12 N on the center of the top plate to both a simple lattice sandwich structure and TSM without preloading. The stress distribution of the lattice structure is highly concentrated, and the maximum von Mises stress reaches up to 8.2 MPa. The deformation in non-tensegrity structure is localized and hard to spread transversely. In contrast, the deformation of TSM was highly uniform, and the stress was evenly distributed within the structure, which decreases the maximum von Mises stress to 0.3 MPa. Even under eccentric loading, TSM maintains stability and excellent load distribution capability, as illustrated in Fig. 17. The peripheral cables counterbalance the torque caused by the eccentric loading.

3.4. Tunable dynamic responses

The impact mitigation performance of TSM is investigated by numerical simulations of a cylindrical object crashing into the TSM by free fall. The cylindrical object had a radius of 9 mm and a height of 25 mm, weighing 50 g. Fig. 18 (a and b) present the keyframes during the experiment and simulation with a falling height of 64.5 mm. The cylindrical object collides and rebounds several times before it finally stops on the metamaterial. In the experiment, given that the bottom plate was not fixed to the ground, part of the impact energy was absorbed by TSM's dynamic energy. TSM rebounded together with the cylindrical object into the air, which decreased the rebound height of the cylindrical object. Both the experiment and simulation show good recoverability and energy dissipation of TSM. Fig. 18 (c-e) shows the dynamic responses of the TSM during impact from simulations. The cylindrical object's rebound height, impact velocity, and contact force decrease gradually. The impact induces oscillation of the TSM, but the oscillation dampens rapidly.

Compared with the previous quasi-static analysis, the quasi-static compression represents a single maximum-value compression, while the dynamic test undergoes multiple and decreasing cyclic compressions. The impact energy is dissipated gradually by TSM. Due to the

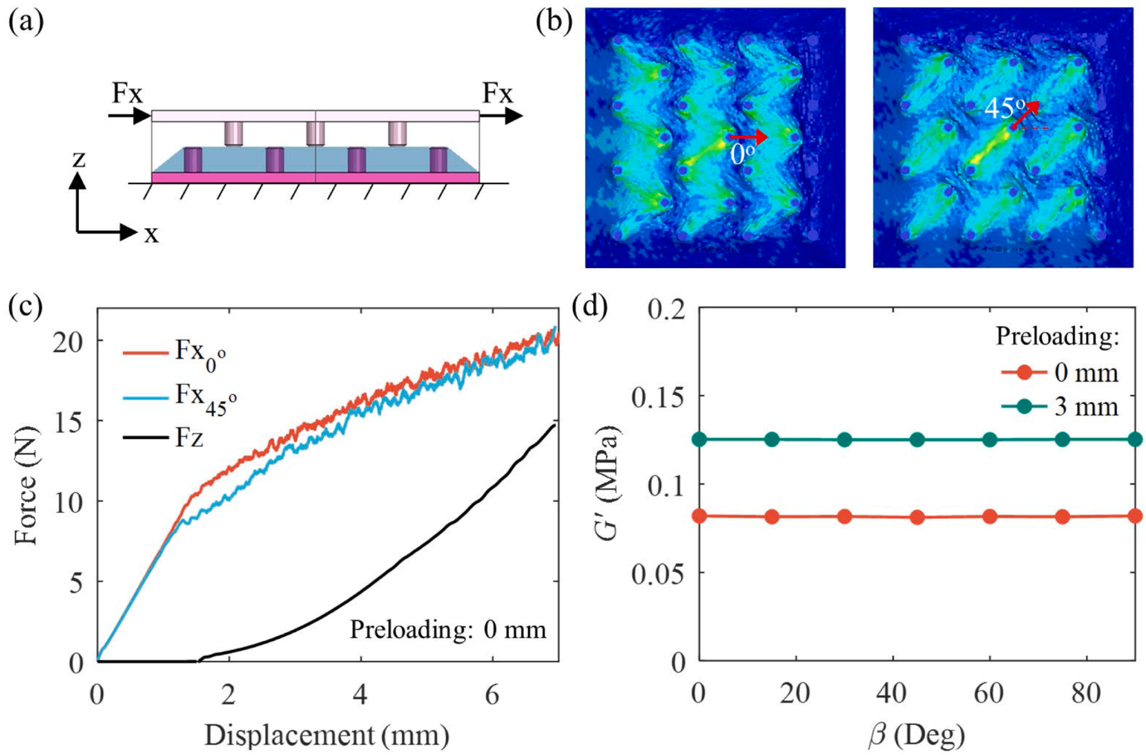

Fig. 15. Shear deformation behavior of TSM. (a) Simulation setup. (b) Numerical deformation of membrane at 0° and 45° shear direction. (c) Comparison of in-plane shear force and out-of-plane compression force. (d) Shear moduli at different shear directions and preloading.

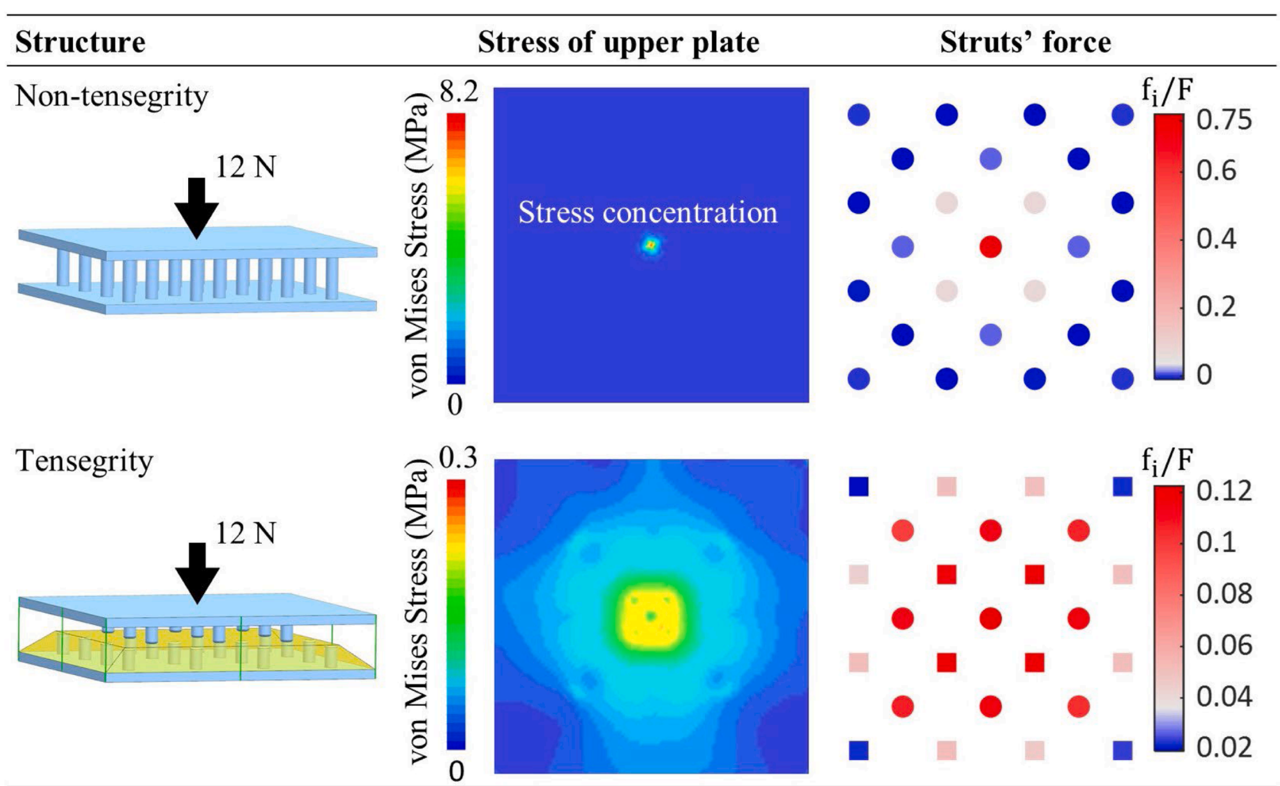

Fig. 16. Comparison between a simple lattice sandwich structure and TSM. Numerical simulations are conducted by applying a load of 12 N on the center of the upper plate. The von Mises stress distribution of the upper plates and the force distribution within struts are shown on the right.

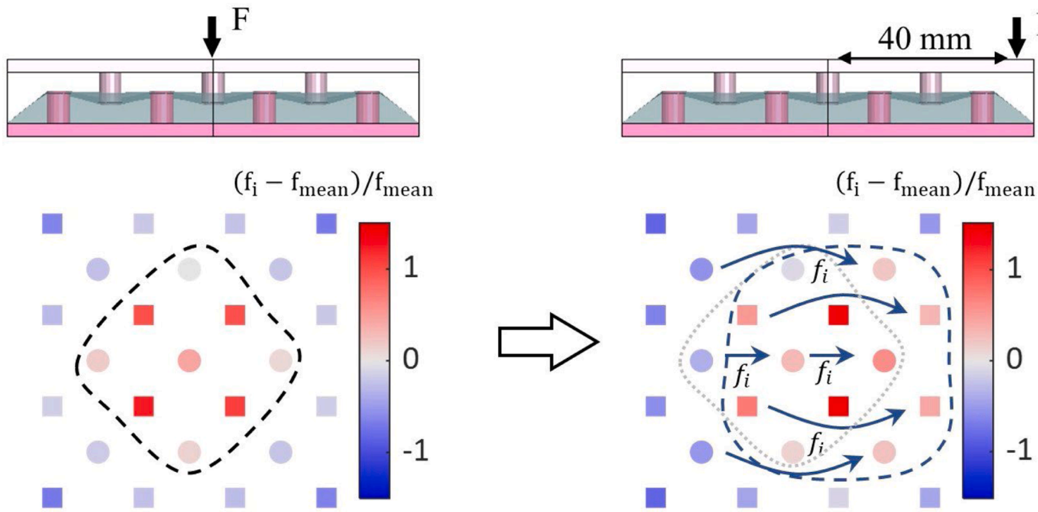

Fig. 17. Deviation of strut force under point load. The point load is first located at the center of the TSM and then moved to the right edge. TSM is preloaded 3 mm and compressed 4 mm by the point load.

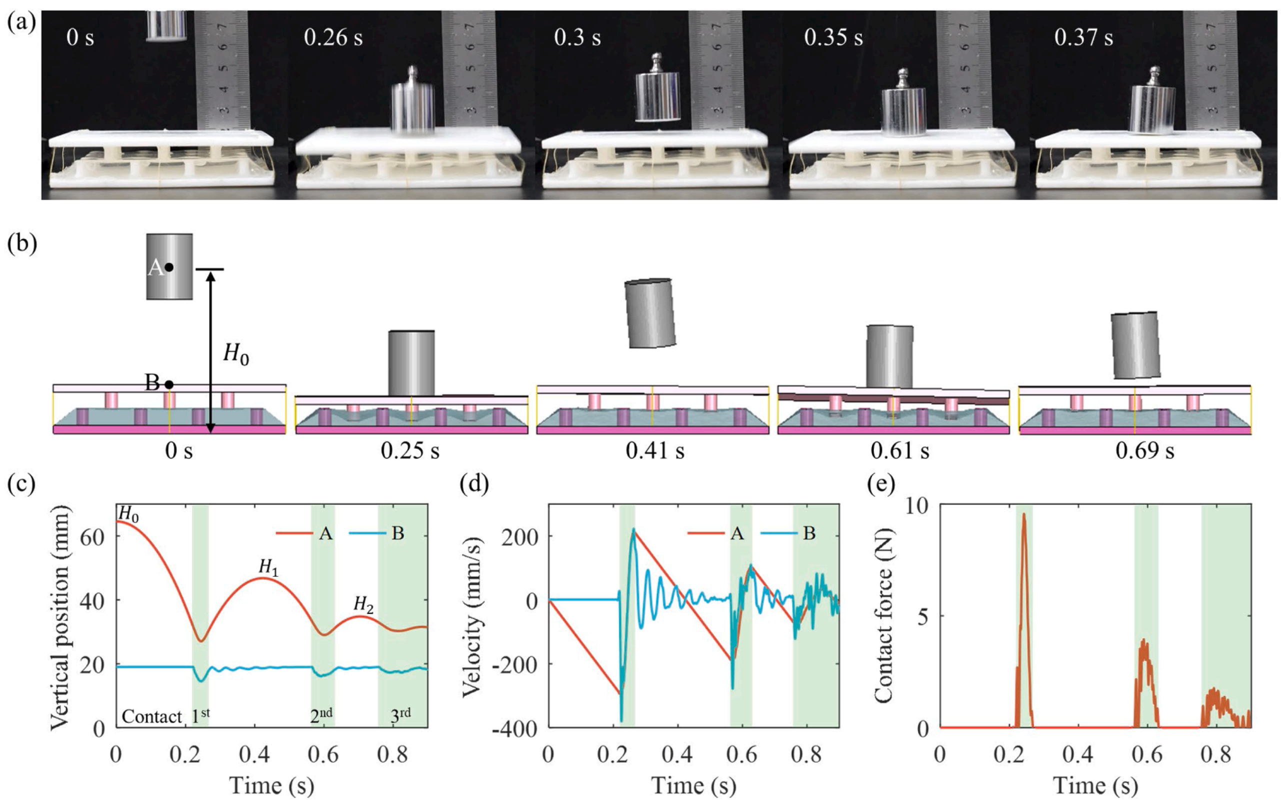

Fig. 18. Impact resistance of the TSM. (a) and (b) Snapshots of the impact process from experiment and simulation. The cylindrical object falls from a certain height. The TSM is preloaded 1 mm. Variation of (c) vertical positions, (d) impact velocity, and (e) contact force during impact. The curves are tracked from the center of gravity of the cylindrical object and the upper surface of the TSM. The green shades highlight the duration of a contact.

object finally stopping at the surface of TSM, the dynamic energy dissipation capacity is only related to the maximum loading curve. In contrast, the quasi-static energy dissipation must consider the unloading curve. As a result, the energy dissipation in dynamics is larger than that of the quasi-static.

The tunable dynamic properties of the TSM are demonstrated in Fig. 19. Here, the symbol Δ denotes the distance between the cylindrical object's bottom surface and the TSM's top surface. The distance Δ ranges from 3 to 33 mm in numerical simulations. The TSM also exhibits excellent tunability for the dynamic response. For example, we can customize a constant impact force or velocity corresponding to different falling heights, as shown in Fig. 19 (a and b). Fig. 19 (c and d) depicts the energy dissipation of TSM at the first and second collisions. A high preloading distance mitigates the influence of falling distance, leading to nearly constant energy dissipation.

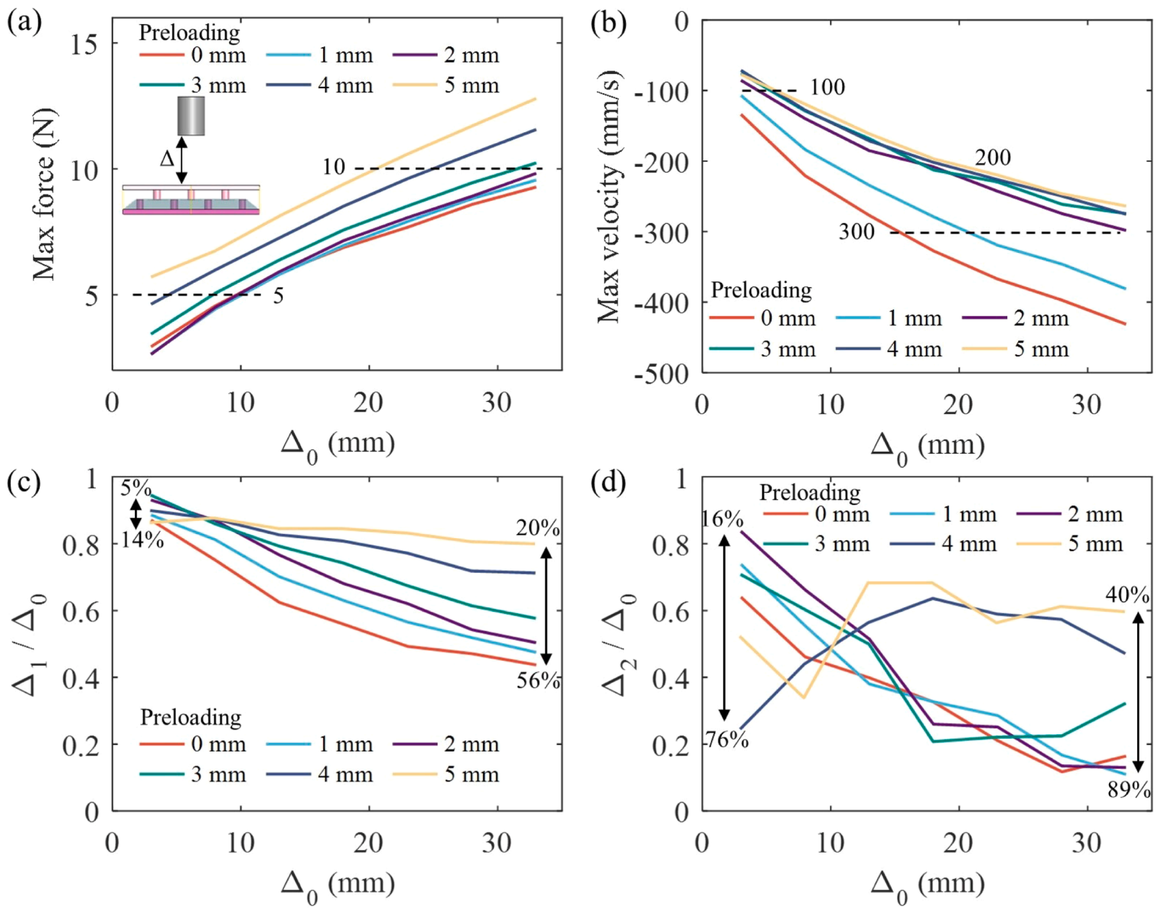

Fig. 19. Simulation results for the reprogrammable dynamic response of TSM by preloading. (a) Max impact force and (b) max impact velocity versus falling distance. The symbol Δ denotes the falling distance of the cylindrical object. (c, d) Energy dissipation versus falling distance. The symbols Δ_1 and Δ_2 denote the rebounding height after the first and second collisions. The ratio of rebounding height and initial height represents the dissipated energy.

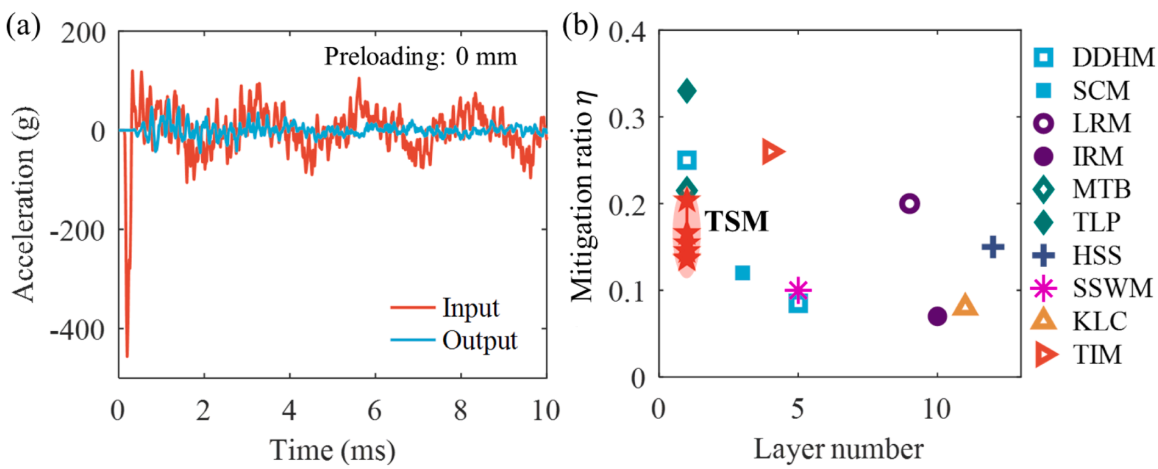

Fig. 20. (a) Simulation results of the input and output acceleration wave time history diagram. (b) Comparison of the mitigation efficiency of TSM with existing metamaterials.

3.5. Comparison of impact mitigation capability

The impact mitigation capability of a metamaterial is evaluated by mitigation ratio η. The lower the η, the better the impact energy mitigation capacity of metamaterials. The mitigation ratio η is defined as the ratio between maximum output acceleration and maximum input acceleration [60,79,80]. Here, the acceleration of the upper and bottom plate of TSM was recorded from the dynamic simulations as the input and output acceleration, as shown in Fig. 20 (a). The mitigation ratio η of TSM without preloading is 0.136.

Subsequently, in Fig. 20 (b), the mitigation ratio of TSM was compared with that of DNA-inspired double helical metamaterials (DDHM) [80], syndiotactic chiral metamaterials (SCM) [81], local resonant metamaterials (LRM) [82], internal resonator metamaterials

(IRM) [79], meta-panel bars (MTB) [83], tri-layer polymers (TLP) [84], hollow spherical structures (HSS) [85], sandwich-structure woodpile metamaterials (SSWM) [86], Kirigami lantern chains (KLC) [87], and tensegrity-inspired metamaterials (TIM) [60]. TSM can achieve a high mitigation ratio through a single-layer structure and tune the mitigation ratio within the range of 0.136-0.204.

4. Conclusions

This work presents a tensegrity-inspired sandwich metamaterial (TSM) designed for reprogrammable mechanical properties and efficient fabrication. The TSM is successfully fabricated by assembling ropes, an elastic membrane, and spiked plates. An analytical model is established to investigate the tunable stiffness of TSM. Through finite element analysis and experiments, the mechanical behavior of the TSM is analyzed, including deformation modes, stiffness, load distribution, and dynamic impact mitigation.

TSM realizes a virtual network of tensile forces by the surface deformation of the continuum membrane. This virtual tensile network offers excellent stress distribution and delocalized deformation capacities, solving the stress concentration problem under localized loading. Peripheral cables are used to provide convenient prestress adjustment. Through adjusting the length of the peripheral cables, TSM exhibits a highly tunable range of properties, reaching 50% of its height, that changes its stiffness in a large range, such as zero, progressive, and constant stiffness. Consequently, the energy dissipation efficiency of the TSM is tunable within the range of 20%-56%. Finally, the TSM achieves a high mitigation ratio up to 0.136.

The TSM demonstrates significant potential for applications in impact mitigation and adaptive structural systems. Its ability to customize static and dynamic responses offers possibilities for new protective materials and systems. However, if the compression distance of the current TSM exceeds 50% of height, it faces the buckling of struts and may lose the tuning capacity. Moreover, the current TSM can only dissipate energy under unidirectional compression, but lacks the energy dissipation capacity under tension direction. Future work could consider incorporating multi-material designs, employing machine learning techniques to optimize the structural topology for specific mechanical properties, or substituting cables with superelastic components to improve impact mitigation and vibration control. Overall, this research establishes a foundation for further exploration into reprogrammable and robotic metamaterials, exhibiting great potential applications in many engineering fields, including civil, mechanical, and aerospace engineering.

CRediT authorship contribution statement

Bowen Tan: Writing – original draft, Methodology, Investigation, Conceptualization. **Bushra Jawed:** Writing – review & editing, Validation. **Ke Liu:** Writing – review & editing, Validation, Supervision, Funding acquisition.

Declaration of competing interest

The authors declare that they have no known competing financial interests or personal relationships that could have appeared to influence the work reported in this paper.

Acknowledgments

This research is supported by the National Natural Science Foundation of China through grant 12372159, the National Key Research and Development Program of China through grant 2022YFB4701900, and the Fundamental Research Funds for the Central Universities, Peking University.

Data availability

Data will be made available on request.

References

[1] Veuve N, Safaei SD, Smith IFC. Deployment of a tensegrity footbridge. J Struct Eng 2015;141.
[2] Pietroni N, Tarini M, Vaxman A, Panozzo D, Cignoni P. Position-based tensegrity design. Acm T Graphic 2017;36.
[3] Xu YY, Chen MH. The minimal mass tensegrity solutions to compressive and tensile loads. Int J Mech Sci 2025;286.
[4] Feng XD, Xu J, Zhang JY, Ohsaki M, Zhao Y, Luo YZ, Chen Y, Xu X. Trajectory planning on rolling locomotion of spherical movable tensegrity robots with multi-gait patterns. Soft Robot 2024;11:725–40.
[5] R.B. Fuller, Tensile-integrity structures, in, United States Patent 3063521, 1962.
[6] Fabbrocino F, Modano N, Farina I, Carpentieri G, Fraternali F. Optimal prestress design of composite cable-stayed bridges. Compos Struct 2017;169:167–72.
[7] Cimmino MC, Miranda R, Sicignano E, Ferreira AJM, Skelton RE, Fraternali F. Composite solar facades and wind generators with tensegrity architecture. Compos Part B-Eng 2017;115:275–81.
[8] Caluwaerts K, Despraz J, Işçen A, Sabelhaus AP, Bruce J, Schrauwen B, SunSpiral V. Design and control of compliant tensegrity robots through simulation and hardware validation. J R Soc Interface 2014;11.
[9] Rimoli JJ. A reduced-order model for the dynamic and post-buckling behavior of tensegrity structures. Mech Mater 2018;116:146–57.
[10] Zhang JY, Ohsaki M, Rimoli JJ, Kogiso K. Optimization for energy absorption of 3-dimensional tensegrity lattice with truncated octahedral units. Compos Struct 2021;267.
[11] Schenk M, Guest SD, Herder JL. Zero stiffness tensegrity structures. Int J Solids Struct 2007;44:6569–83.
[12] Liu CY, Li K, Yu XZ, Yang JP, Wang ZJ. A multimodal self-propelling tensegrity structure. Adv Mater 2024.
[13] Liu K, Wu JT, Paulino GH, Qi HJ. Programmable deployment of tensegrity structures by stimulus-responsive polymers. Sci Rep-Uk 2017;7.
[14] Dong YC, Yuan XF, Ma S, Li S, Samy A, Dong SL. Research on a novel tensegrity torus with superior shape adaptability. Structures 2024;63.
[15] Micheletti A, Podio-Guidugli P. Seventy years of tensegrities (and counting). Arch Appl Mech 2022;92:2525–48.
[16] Carreño F, Post MA. Design of a novel wheeled tensegrity robot: a comparison of tensegrity concepts and a prototype for travelling air ducts. Robot Biomimet 2018; 5:1.
[17] Skelton RE, Fraternali F, Carpentieri G, Micheletti A. Minimum mass design of tensegrity bridges with parametric architecture and multiscale complexity. Mech Res Commun 2014;58:124–32.
[18] Ganga PL, Micheletti A, Podio-Guidugli P, Scolamiero L, Tibert G, Zolesi V. Tensegrity rings for deployable space antennas: concept, design, analysis, and prototype testing. Springer Optim Appl 2016;116:269–304.
[19] Zhang GT, Chen MH, Chen DH, Shen YL. Lightweight designs of simply supported tensegrity structures and their applications to bridges. Compos Struct 2025;357.
[20] Nian YZ, Wan S, Avcar M, Yue R, Li M. 3D printing functionally graded metamaterial structure: design, fabrication, reinforcement, optimization. Int J Mech Sci 2023;258.
[21] Nian YZ, Wan S, Wang X, Zhou P, Avcar M, Li M. Study on crashworthiness of nature-inspired functionally graded lattice metamaterials for bridge pier protection against ship collision. Eng Struct 2023;277.
[22] Nian YZ, Wan S, Avcar M, Wang X, Hong R, Yue R, Li M. Nature-inspired 3D printing-based double-graded aerospace negative Poisson's ratio metastructure: design, Fabrication, Investigation, optimization. Compos Struct 2024;348.
[23] Davami K, Rowe R, Gulledge B, Park J, Beheshti A, Palazotto A, Tavangarian F, Beck S. Dynamic analysis of additively manufactured tensegrity structures. Int J Impact Eng 2025;198.
[24] Chen YQ, Dong YC, Yuan XF, Ma S, Dong SL. Modular assembly of tensegrity structures with diverse mesh division forms. Eng Struct 2024;315.
[25] Jiang JH, Yin X, Xu GK, Wang ZY, Zhang LY. A unified analytical form-finding of truncated regular octahedral tensegrities. Int J Mech Sci 2023;239.
[26] Zhang JY, Ohsaki M. Stability conditions for tensegrity structures. Int J Solids Struct 2007;44:3875–86.
[27] Xu ZY, Lu JY, Wu JR, Liu JL, Gu X, Li N. A computational method to find the optimal driving-path for stable state transformation of multistable tensegrity. Comput Struct 2025;310.
[28] Ma S, Chen MH. Stability conditions of tensegrity structures considering local and global buckling. Int J Mech Sci 2025;287.
[29] Liu K, Paulino GH. Tensegrity topology optimization by force maximization on arbitrary ground structures. Struct Multidiscip O 2019;59:2041–62.
[30] Tracy K, Gupta S, Stella Y, Wen S, Wortmann T, Bamford R. Tensile configurations: exploring spatial membrane tensegrity shell structures. In: Proceedings of the ACADIA 2019; 2019.
[31] Gupta SS, Tan YY, Chia PZ, Pambudi CP, Quek YH, Yogiaman C, Tracy KJ. Prototyping knit tensegrity shells: a design-to-fabrication workflow. Sn Appl Sci 2020;2.
[32] Palmieri M, Giannetti I, Micheletti A. Floating-bending tensile-integrity structures. Curved Layer Struct 2021;8:89–95.

[33] Fraddosio A, Pavone G, Piccioni MD. Minimal mass and self-stress analysis for innovative V-Expander tensegrity cells. Compos Struct 2019;209:754–74.
[34] Fraddosio A, Pavone G, Piccioni MD. A novel method for determining the feasible integral self-stress states for tensegrity structures. Curved Layer Struct 2021;8: 70–88.
[35] Yue XH, Yin X, Sun ZY, Liu LY, Wang YT, Xu GK, Cao CY, Zhang LY. Flexible, lightweight, tunable robotic arms enabled by X-tensegrity inspired structures. Compos Struct 2024;344.
[36] Rimoli JJ, Pal RK. Mechanical response of 3-dimensional tensegrity lattices. Compos Part B-Eng 2017;115:30–42.
[37] Lee S, Gan BS, Lee J. A fully automatic group selection for form-finding process of truncated tetrahedral tensegrity structures via a double-loop genetic algorithm. Compos Part B-Eng 2016;106:308–15.
[38] Cai JG, Wang XY, Deng XW, Feng J. Form-finding method for multi-mode tensegrity structures using extended force density method by grouping elements. Compos Struct 2018;187:1–9.
[39] Intrigila C, Micheletti A, Nodargi NA, Artioli E, Bisegna P. Fabrication and experimental characterisation of a bistable tensegrity-like unit for lattice metamaterials. Addit Manuf 2022;57.
[40] Lee S, Lee J. Advanced automatic grouping for form-finding of tensegrity structures. Struct Multidiscip O 2017;55:959–68.
[41] Xu X, Wang YF, Luo YZ. General approach for topology-finding of tensegrity structures. J Struct Eng 2016;142.
[42] Guest SD. The stiffness of tensegrity structures. Ima J Appl Math 2011;76:57–66.
[43] Korkmaz S, Ali NBH, Smith IFC. Configuration of control system for damage tolerance of a tensegrity bridge. Adv Eng Inform 2012;26:145–55.
[44] Cai JG, Yang RG, Wang XY, Feng J. Effect of initial imperfections of struts on the mechanical behavior of tensegrity structures. Compos Struct 2019;207:871–6.
[45] Chen Y, Feng J, Lv HZ, Sun QZ. Symmetry representations and elastic redundancy for members of tensegrity structures. Compos Struct 2018;203:672–80.
[46] Song KY, Scarpa F, Schenk M. Manufacturing sensitivity study of tensegrity structures using Monte Carlo simulations. Int J Solids Struct 2024;298.
[47] Al Sabouni-Zawadzka A, Gilewski W, Charandabi RN, Zawadzki A. Stability of tensegrity-inspired structures fabricated through additive manufacturing. Compos Struct 2024;345.
[48] Amendola A, Krushynska A, Daraio C, Pugno NM, Fraternali F. Tuning frequency band gaps of tensegrity mass-spring chains with local and global prestress. Int J Solids Struct 2018;155:47–56.
[49] Micheletti A, Ruscica G, Fraternali F. On the compact wave dynamics of tensegrity beams in multiple dimensions. Nonlinear Dynam 2019;98:2737–53.
[50] Fraternali F, Senatore L, Daraio C. Solitary waves on tensegrity lattices. J Mech Phys Solids 2012;60:1137–44.
[51] Fraternali F, Carpentieri G, Amendola A. On the mechanical modeling of the extreme softening/stiffening response of axially loaded tensegrity prisms. J Mech Phys Solids 2015;74:136–57.
[52] Motta JD, Garanger K, Rimoli JJ. Propagation of compression solitary waves on tensegrity-like lattices made of truncated octahedrons. Int J Nonlin Mech 2024; 162.
[53] Yazbeck R, El-Borgi S, Boyd JG, Chen M, Lagoudas DC. Non-dimensional linear analysis of one-dimensional wave propagation in tensegrity structures. Compos Struct 2025;353.
[54] Zhang LY, Yin X, Yang J, Li A, Xu GK. Multilevel structural defects-induced elastic wave tunability and localization of a tensegrity metamaterial. Compos Sci Technol 2021;207.
[55] Yin X, Zhang S, Xu GK, Zhang LY, Gao ZY. Bandgap characteristics of a tensegrity metamaterial chain with defects. Extreme Mech Lett 2020;36.
[56] Yin X, Gao ZY, Zhang S, Zhang LY, Xu GK. Truncated regular octahedral tensegrity-based mechanical metamaterial with tunable and programmable Poisson's ratio. Int J Mech Sci 2020;167.
[57] Salahshoor H, Pal RK, Rimoli JJ. Material symmetry phase transitions in three-dimensional tensegrity metamaterials. J Mech Phys Solids 2018;119:382–99.
[58] Li A, Yin X, Guan B, Xu GK, Zhang LY, Feng XQ. A configurable tensegrity-based metastructure with tunable bandgap achieved by structural phase transition. Thin Wall Struct 2025;209.
[59] Wang YT, Zhao WJ, Rimoli JJ, Zhu R, Hu GK. Prestress-controlled asymmetric wave propagation and reciprocity-breaking in tensegrity metastructure. Extreme Mech Lett 2020;37.
[60] Zeng H, Mu RA, Huo KY, Zhao HF, Wang K, Wang AP. A novel 3D-printable tensegrity-inspired metamaterial enabling dynamic attenuation. Int J Mech Mater Des 2023;19:883–901.
[61] Amendola A. An analytic study on the properties of solitary waves traveling on tensegrity-like lattices. Int J Nonlin Mech 2023;148.
[62] Feron J, Latteur P. Implementation and propagation of prestress forces in pin-jointed and tensegrity structures. Eng Struct 2023;289.
[63] Habibi T, Rhode-Barbarigos L, Keller T. Effects of prestress implementation on self-stress state in large-scale tensegrity structure. Eng Struct 2023;288.
[64] Liu K, Zegard T, Pratapa PP, Paulino GH. Unraveling tensegrity tessellations for metamaterials with tunable stiffness and bandgaps. J Mech Phys Solids 2019;131: 147–66.
[65] Cheng HW, Zhu XX, Cheng XW, Cai PZ, Liu J, Yao HJ, Zhang L, Duan JL. Mechanical metamaterials made of freestanding quasi-BCC nanolattices of gold and copper with ultra-high energy absorption capacity. Nat Commun 2023;14.
[66] Cesnik M, Slavic J, Boltezar M. Accelerated vibration-fatigue characterization for 3D-printed structures: application to fused-filament-fabricated PLA samples. Int J Fatigue 2023;171.
[67] Cesnik M, Slavic J. Temperature-amplitude spectrum for early full-field vibration-fatigue-crack identification. Int J Mech Sci 2025;286.
[68] Lee H, Jang Y, Choe JK, Lee S, Song H, Lee JP, Lone N, Kim J. 3D-printed programmable tensegrity for soft robotics. Sci Robot 2020;5.
[69] Santos FA, Caroco C, Amendola A, Miniaci M, Fraternali F. 3d tensegrity braces with superelastic response for seismic control. Int J Multiscale Com 2022;20: 53–64.
[70] Bauer J, Kraus JA, Crook C, Rimoli JJ, Valdevit L. Tensegrity metamaterials: toward failure-resistant engineering systems through delocalized deformation. Adv Mater 2021;33.
[71] Yang H, Zhang J, Wang J, Hu JB, Wu ZG, Pan F, Wu JN. Delocalized deformation enhanced reusable energy absorption metamaterials based on bistable tensegrity. Adv Funct Mater 2024.
[72] Zhang Y, Zheng K, Zhao Y, Zheng Z, Chen B, Chen M. Collision resistant study of spherical tensegrity structures for protective drone shells. Extreme Mech Lett 2025; 76:102312.
[73] Pajunen K, Johanns P, Pal RK, Rimoli JJ, Daraio C. Design and impact response of 3D-printable tensegrity-inspired structures. Mater Design 2019;182.
[74] Santos FA. Toward a novel energy-dissipation metamaterial with tensegrity architecture. Adv Mater 2023;35.
[75] Feng XD, Shen J, Zhao WY, Lyu H, Su YQ. A novel method for optimizing energy absorption of tensegrities with multi-self-stress modes. Structures 2024;64.
[76] Zhang QC, Zhang DY, Dobah Y, Scarpa F, Fraternali F, Skelton RE. Tensegrity cell mechanical metamaterial with metal rubber. Appl Phys Lett 2018;113.
[77] Filipov ET, Liu K, Tachi T, Schenk M, Paulino GH. Bar and hinge models for scalable analysis of origami. Int J Solids Struct 2017;124:26–45.
[78] Wei ZB, Hu Z, Zhu R, Chen Y, Hu GK. A transformable anisotropic 3D penta-mode metamaterial. Mater Design 2023;234.
[79] Khan MH, Li B, Tan KT. Impact load wave transmission in elastic metamaterials. Int J Impact Eng 2018;118:50–9.
[80] Hu JX, Yu TX, Yin S, Xu J. Low-speed impact mitigation of recoverable DNA-inspired double helical metamaterials. Int J Mech Sci 2019;161.
[81] Ou HF, Hu LL, Wang YB, Liu C. High-efficient and reusable impact mitigation metamaterial based on compression-torsion coupling mechanism. J Mech Phys Solids 2024;186.
[82] Zhou YC, Ye L, Chen Y. Investigation of novel 3D-printed diatomic and local resonant metamaterials with impact mitigation capacity. Int J Mech Sci 2021;206.
[83] Vo NH, Pham TM, Hao H, Bi KM, Chen WS. Experimental and numerical validation of impact mitigation capability of meta-panels. Int J Mech Sci 2022;231.
[84] Sonnenschein MF, Nicoli E, Ma LK, Wendt BL. Impact mitigation in layered polymeric structures. Polymer 2017;131:25–33.
[85] Yin S, Chen DH, Xu J. Novel propagation behavior of impact stress wave in one-dimensional hollow spherical structures. Int J Impact Eng 2019;134.
[86] Hwang HY, Lee JW, Yang J, Shul CW, Kim E. Sandwich-Structured Woodpile Metamaterials for Impact Mitigation. Int J Appl Mech 2018;10.
[87] Zhang W, Xu J. Ultra-light kirigami lantern chain for superior impact mitigation. Extreme Mech Lett 2022;51.